43rd AIAA Aerospace Sciences Meeting, 10-13 January 2005, Reno Nevada

Computational Studies of High-Speed Flow Control with Weakly-Ionized Plasma

Jonathan Poggie*

Air Force Research Laboratory, Wright-Patterson AFB, OH 45433-7512 USA

A numerical study of glow discharges was carried out in order to evaluate their potential for flow control applications. As part of this project, a three-dimensional computer code has been written to solve, in an implicit, loosely-coupled fashion, the fluid conservation laws, the charged particle continuity equations under the drift-diffusion model, and the Poisson equation for the electric potential. Fully three-dimensional calculations have been carried out for DC discharges in nitrogen, and changes in the flow in the presence a discharge have been demonstrated. In computations of a three-dimensional electrode configuration mounted on a flat plate in a Mach 5 crossflow, the discharge was found to thicken the boundary layer. The resulting compression waves led to increased pressure forces at the plate surface. These changes in flow structure occurred through dissipative heating; the body force term in the fluid momentum equation was negligible. Analogous, but less dramatic, effects were observed for electrodes mounted on a NACA-0012 airfoil in low-speed flow. Here the net result was a decrease in the lift-to-drag ratio on the airfoil. A preliminary investigation of the effect of an applied magnetic field has also been carried out. A computation of a simple discharge between parallel plates showed that an applied axial magnetic field tends to suppress the radial component of the current density and introduce a small swirl component.

I. Introduction

Plasma actuators are currently considered to be a promising means of flow control.[1–8] A number of different plasma generation methods have been considered for flow control schemes, including DC glow discharges, RF glow discharges, and dielectric barrier discharges, and control experiments have been carried out both with and without the presence of an applied magnetic field. Significant control effects have been observed in experiments on both high-speed[6,7] and low-speed flow.[3,4] Accurate modeling of such flow control devices, however, requires consideration of many physical phenomena, particularly space charge effects or sheaths, which are not typically incorporated into conventional fluid dynamics models.

Over the past few years, a prototype code (`PS3D`) has been written in order to model flow in the presence of finite space charge effects, and examine the plasma sheaths present near electrode surfaces.[9–16] The current version of the code is three-dimensional, and includes the capability to model the effects of an applied magnetic field. Options are present in the code to model the motion of each species of charged particle with continuity/momentum equations appropriate to a low-density regime[14,16] or with a drift-diffusion equation appropriate to a high-density regime.[13,15]

The higher density regime is the focus of the present work, which is aimed at developing a capability to simulate experiments with plasma actuators. Earlier efforts considered simple two-dimensional, direct-current glow discharges,[13] then moved on to more complicated geometries with uncoupled fluid mechanics.[15]

*Research Aerospace Engineer, AFRL/VAAC, Bldg. 146 Rm. 225, 2210 Eighth St. Associate Fellow AIAA.

Here, fully-coupled, three-dimensional cases are considered, and preliminary investigations of the effect of an applied magnetic field are presented. Calculations of DC glow discharges in nitrogen have been carried out for three configurations: a simple discharge between parallel plates, a discharge for a three-dimensional electrode configuration mounted on a flat plate in a Mach 5 flow, and a discharge between electrodes mounted on a NACA-0012 airfoil in a low-speed flow.

II. Methods

An implicit, loosely-coupled method is employed to solve the fluid conservation laws, the charged particle continuity equations under the drift-diffusion model, and the Poisson equation for the electric potential. The physical model and numerical procedure are described in this section.

A. Physical Model

The conservation of mass, momentum, and energy for the overall gas is expressed as:

$$\frac{\partial \rho}{\partial t} + \nabla \cdot (\rho \mathbf{u}) = 0 \tag{1}$$

$$\frac{\partial}{\partial t}(\rho \mathbf{u}) + \nabla \cdot (\rho \mathbf{u}\mathbf{u} - \boldsymbol{\Sigma}) = \rho_c \mathbf{E} + \mathbf{j} \times \mathbf{B} \tag{2}$$

$$\frac{\partial \mathcal{E}}{\partial t} + \nabla \cdot (\mathbf{u}\mathcal{E} - \boldsymbol{\Sigma} \cdot \mathbf{u} + \mathbf{Q}) = \mathbf{E} \cdot \mathbf{j} \tag{3}$$

where the total fluid energy is defined as $\mathcal{E} = \rho(\epsilon + u^2/2)$. The mass density, the charge density, and the total current density are found by summing over all species: $\rho = \Sigma_s m_s n_s$, $\rho_c = \Sigma_s q_s n_s$, and $\mathbf{j} = \Sigma_s q_s n_s \mathbf{v}_s$.

At present, a vibrational energy equation is not incorporated into the model. Following the simplified treatment of vibrational nonequilibrium commonly used in the literature,[17] the energy deposition term $\mathbf{E} \cdot \mathbf{j}$ in Eq. (3) is replaced with $\eta \mathbf{E} \cdot \mathbf{j}$, where $1 - \eta$ represents the fraction of energy delivered to vibrational modes. Here we take $\eta = 0.1$.

The total stress tensor $\boldsymbol{\Sigma}$ is given by the usual constitutive equation for a Newtonian fluid and the heat flux $\mathbf{Q}$ follows Fourier's heat conduction law:

$$\Sigma_{ij} = -p\delta_{ij} + \mu \left(\frac{\partial u_i}{\partial x_j} + \frac{\partial u_j}{\partial x_i} \right) - \frac{2}{3}\mu \frac{\partial u_k}{\partial x_k} \delta_{ij} \tag{4}$$

$$Q_i = -k \frac{\partial T}{\partial x_i} \tag{5}$$

where μ and k are, respectively, the viscosity and thermal conductivity. The transport coefficients were evaluated using the correlations given in Ref. 18.

Neglecting acceleration terms and diffusion due to temperature gradients, the particle and momentum conservation equations for each species can be combined to obtain a drift-diffusion model:

$$\frac{\partial n_s}{\partial t} + \nabla \cdot \{ n_s \left[\mathbf{u} + s_s \mu_s \mathbf{M}^s \cdot (\mathbf{E} + \mathbf{u} \times \mathbf{B}) \right] \} = \nabla \cdot (D_s \mathbf{M}^s \cdot \nabla n_s) + \omega_s \tag{6}$$

where s_s is the sign of q_s, and the tensor $\mathbf{M}^s$ is defined as:

$$M^s_{ij} = \frac{1}{1 + \mu_s^2 B^2} \left(\delta_{ij} + \mu_s^2 B_i B_j + s_s \mu_s \epsilon_{ijk} B_k \right) \tag{7}$$

The dot product in Eq. (6) corresponds to summation on the second index of M_{ij}.

For later use, we define several quantities related to the species velocity:

$$\mathbf{V}_s = \mathbf{u} + s_s \mu_s \mathbf{M}^s \cdot (\mathbf{E} + \mathbf{u} \times \mathbf{B}) \quad (8)$$

$$\mathbf{\Gamma}_s = n_s s_s \mu_s \mathbf{M}^s \cdot (\mathbf{E} + \mathbf{u} \times \mathbf{B}) - D_s \mathbf{M}^s \cdot \nabla n_s \quad (9)$$

$$\mathbf{w}_s = \mathbf{\Gamma}_s / n_s \quad (10)$$

$$\mathbf{v}_s = \mathbf{u} + \mathbf{w}_s \quad (11)$$

These are, respectively, a convection-drift velocity (8), a species flux relative to the bulk flow (9), a corresponding species velocity (10), and a total species velocity (11).

For the present work, two species of charged particles are considered (ions and electrons, denoted below by subscript i and e), and the charged particle generation rate is taken to have the form:

$$\omega_{i,e} = \alpha \Gamma_e - \beta n_i n_e \quad (12)$$

where α is the ionization coefficient, β is the recombination coefficient, and Γ_e is the magnitude of the electron flux. All the discharge calculations presented in this paper were carried out for nitrogen gas. Data for the mobilities, diffusion coefficients, ionization coefficient, and recombination coefficient were taken from Ref. 19.

The electric potential is determined from the Poisson equation:

$$\nabla^2 \phi = -\rho_c / \epsilon_0 \quad (13)$$

where ϵ_0 is the permittivity of free space, and the electric field is found from $\mathbf{E} = -\nabla\phi$.

Conventional no-slip wall conditions and inlet/outlet boundary conditions were used for the fluid equations. The normal component of the ion flux was assumed to be zero at the anode, and the normal component of the electron flux at the cathode was found from the relation:

$$\mathbf{\Gamma}_e \cdot \mathbf{n} = -\gamma \mathbf{\Gamma}_i \cdot \mathbf{n} \quad (14)$$

where γ is the secondary emission coefficient, $\mathbf{n}$ is a unit normal vector, and the species fluxes $\mathbf{\Gamma}_{i,e}$ were computed using one-sided, second-order spatial differences. The potential at the anode was taken to be zero. The cathode potential V_c was either held fixed, or determined according to an external circuit such that $V_c = -V + IR$, where V is the applied voltage, R is the external resistance, and I is the total current at the anode.

B. Numerical Methods

The conservation laws were solved using approximately-factored, implicit schemes, related to those developed by Beam and Warming,[20] Pulliam,[21] and Surzhikov and Shang.[19] The conservation equations (1)–(3) and (6) can be written in the form:

$$\frac{\partial U}{\partial t} + \frac{\partial E}{\partial x} + \frac{\partial F}{\partial y} + \frac{\partial G}{\partial z} = \frac{\partial E_v}{\partial x} + \frac{\partial F_v}{\partial y} + \frac{\partial G_v}{\partial z} + S \quad (15)$$

Applying the standard transformation from physical coordinates (x, y, z) to grid coordinates (ξ, η, ζ) gives:

$$\frac{\partial \overline{U}}{\partial t} + \frac{\partial \overline{E}}{\partial \xi} + \frac{\partial \overline{F}}{\partial \eta} + \frac{\partial \overline{G}}{\partial \zeta} = \frac{\partial \overline{E}_v}{\partial \xi} + \frac{\partial \overline{F}_v}{\partial \eta} + \frac{\partial \overline{G}_v}{\partial \zeta} + \overline{S} \quad (16)$$

where, for example, $\overline{U} = U/J$ and $\overline{E} = (\xi_x E + \xi_y F + \xi_z G)/J$.

Writing Eq. (16) as $\partial \overline{U}/\partial t = R$, and discretizing in time, we have:

$$(1+\theta)\overline{U}^{n+1} - (1+2\theta)\overline{U}^{n} + \theta \overline{U}^{n-1} = \Delta t R^{n+1} \quad (17)$$

where $\theta = 0$ for an implicit Euler scheme and $\theta = 1/2$ for a three point backward scheme. We introduce subiterations such that $\overline{U}^{n+1} \rightarrow \overline{U}^{p+1}$, with $\Delta\overline{U} = \overline{U}^{p+1} - \overline{U}^{p}$. The right hand side R^{n+1} is linearized in the standard 'thin layer' manner. Collecting the implicit terms on the left hand side, and introducing approximate factoring and a subiteration time step $\Delta\hat{t}$ gives:

$$\begin{aligned}
&\left[I - \frac{\Delta\hat{t}}{1+\theta}(B + \delta_\xi A_1 + \delta_\xi R_1 \delta_\xi + D_{i\xi})\right] \times \\
&\left[I - \frac{\Delta\hat{t}}{1+\theta}(\delta_\eta A_2 + \delta_\eta R_2 \delta_\eta + D_{i\eta})\right] \times \\
&\left[I - \frac{\Delta\hat{t}}{1+\theta}(\delta_\zeta A_3 + \delta_\zeta R_3 \delta_\zeta + D_{i\zeta})\right] \Delta\overline{U} = \\
&- \frac{\Delta\hat{t}}{1+\theta}\left\{\frac{(1+\theta)\overline{U}^p - (1+2\theta)\overline{U}^n + \theta\overline{U}^{n-1}}{\Delta t} - R^p - D_e\overline{U}^p\right\}
\end{aligned} \tag{18}$$

where B is the source Jacobian, and A_{1-3} and R_{1-3} are flux Jacobians.

For the bulk fluid conservation laws, the symbols D_i and D_e are, respectively, the implicit and explicit damping operators described by Pulliam.[21] The explicit damping operator uses a nonlinear blend of second- and fourth-order damping.[22] The spatial derivatives are evaluated using second order central differences.

For the drift-diffusion equations, no damping is used. Instead, these equations are discretized in space using a second-order upwind scheme based on the convection-drift velocity $\mathbf{V}_s$ [defined in Eq. (8)]. The minmod limiter is employed. An upwind method was also applied when calculating the species fluxes present in the source terms. (See the discussion of the charged particle generation term in Ref. 19.)

The Poisson equation is solved using an approximately factored implicit scheme, adapted from the approach described by Holst.[23,24] The three-dimensional Poisson equation (13) can be written in the form:

$$\frac{\partial E}{\partial x} + \frac{\partial F}{\partial y} + \frac{\partial G}{\partial z} = S \tag{19}$$

where $E = \partial\phi/\partial x$, $F = \partial\phi/\partial y$, $G = \partial\phi/\partial z$, and $S = -\rho_c/\epsilon_0$. Applying the transformation of coordinates, this becomes:

$$\frac{\partial \overline{E}}{\partial \xi} + \frac{\partial \overline{F}}{\partial \eta} + \frac{\partial \overline{G}}{\partial \zeta} = \overline{S} \tag{20}$$

Following the procedure described by Holst, we introduce an artificial time term:

$$\frac{\partial \phi}{\partial \tau} = L\phi = \frac{\partial \overline{E}}{\partial \xi} + \frac{\partial \overline{F}}{\partial \eta} + \frac{\partial \overline{G}}{\partial \zeta} - \overline{S} \tag{21}$$

and develop a procedure that drives the numerical solution towards $L\phi = 0$. We write $\Delta\phi/\Delta\tau = L\phi^{p+1}$, where $\Delta\phi = \phi^{p+1} - \phi^p$. We then linearize the right hand side using the standard 'thin layer' approach, introduce $\alpha = 1/\Delta\tau$, an over-relaxation parameter ω, and approximate factoring. This gives:

$$\left[1 + \alpha^{-1}(D - \delta_\xi A \delta_\xi)\right]\left[1 - \alpha^{-1}\delta_\eta B \delta_\eta\right]\left[1 - \alpha^{-1}\delta_\zeta C \delta_\zeta\right]\Delta\phi = \omega\alpha^{-1}L\phi^p \tag{22}$$

where D is the source Jacobian and A, B, and C are the flux Jacobians. The spatial derivatives are evaluated using second-order central differences. In order to accelerate convergence, the pseudo-time parameter is varied according to the procedure:

$$\alpha_p = \alpha_H \left(\frac{\alpha_L}{\alpha_H}\right)^{\frac{p-1}{M-1}} \tag{23}$$

where α_L and α_H are the low and high bounds on α_p, and p cycles periodically between 1 and M.

The fluid equations, the drift-diffusion equations, and the Poisson equation are solved in a loosely-coupled fashion inside a subiteration loop intended to drive $\Delta\overline{U}$ and $\Delta\phi$ toward zero. Typically three overall subiterations are employed, with up to one thousand iterations of the Poisson solver within each overall subiteration.

Due to the disparate time scales involved in the fluid dynamic and electromagnetic phenomena occurring in these problems, calculations can be costly in computer time. Efforts have been made to improve the speed of the computations. In the implementation of the factorized schemes, multi-level parallelism is exploited by using both vectorization and multi-threading with OpenMP commands.[25] Further, the code is set up to run in either a time-accurate mode, or with independent time-steps for the different physics modules, which can be useful for accelerating convergence.

III. Glow Discharge between Parallel Plates

Three-dimensional computations of a parallel-plate discharge were carried out in order to study the effect of a strong magnetic field applied along the discharge axis. The computational grid consisted of $61 \times 51 \times 51$ points, distributed over a $20 \times 40 \times 40$ mm rectangular domain, with grid clustering near the electrode surfaces. (A grid resolution study in one dimension showed that the number of points along the discharge axis was sufficient to resolve the discharge structure.) The working gas was nitrogen at a pressure of 670 Pa. For simplicity, the effect of bulk gas flow was not considered, so the bulk gas velocity was set to zero and its temperature held fixed at 293 K.

The potential at the anode was taken to be zero, and the normal derivatives of all variables were set to zero on the side boundaries. The cathode potential V_c was determined according to an external circuit such that $V_c = -V + IR$, where $V = 2$ kV is the applied voltage, $R = 300$ kΩ is the external resistance, and I is the computed total current at the anode. The secondary emission coefficient was taken to be $\gamma = 0.1$.

The basic discharge structure is illustrated in Fig. 1, which shows selected isosurfaces of the ion number density for the baseline case with no applied magnetic field (Fig. 1a), and a case with an applied magnetic field of $B_x = 1$ T (Fig. 1b). The cathode lies in the $x = 0$ m plane, to the left and back in the figures, and the anode lies in the $x = 0.02$ m plane, the nearest face of the displayed domain. The ion number density distribution is qualitatively similar in both cases. The cathode layer is evident as a pill-shaped region of high ion number density, and the positive column appears as a sausage-shaped region along the axis of symmetry. With the application of the magnetic field, the radial extent of the discharge broadens, with a considerably larger cathode spot.

Insight into the reason for the change in structure can be obtained from the current lines shown in Fig. 2. In the baseline case (Fig. 2a), the current lines show a typical behavior for the normal glow regime: the current density is highest at the anode, but the current lines diverge near the cathode and the current density drops. With the application of the magnetic field (Fig. 2b), charged particle motion in the radial direction (across the field lines) is suppressed, forcing the discharge to expand to pass the total current arriving from the anode.

The discharge properties along the centerline are shown in Fig. 3. The ion number density is shown as a thin solid line, the electron number density as a dash-dot-dot line, and the electric potential as a thick solid line. The cathode is at the left and the anode is at the right. The cathode layer is apparent on the left as a region relatively free of electrons, but with a high ion concentration and a strong electric field ($E_x = -\partial\phi/\partial x$). In the center is the quasi-neutral ($n_i \approx n_e$) positive column, with a nearly constant electric field. At right is the anode layer, which, in contrast to the cathode layer, is distinguished by a depletion of ions relative to electrons.

For the baseline case (Fig. 3a), the maximum ion number density in the cathode layer is on the order of 2.2×10^{16} m^{-3}, and the maximum number density in the positive column is about 1×10^{16} m^{-3} for both ions and electrons. With the applied magnetic field (Fig. 3b), the potential distribution remains approximately the same, but the maximum ion concentration in the cathode layer drops to about 1.6×10^{16} m^{-3}, and the charged particle concentration in the positive column drops to roughly 1×10^{15} m^{-3}.

Note that the cathode voltage is almost the same for the two cases: −610 V for the baseline case and −597 V for the case with the applied magnetic field. The corresponding total currents are 4.6 mA and 4.7 mA, respectively.

Corresponding plots for the same discharge properties in the x-y-plane are presented in Figs. 4-5. In the number density plots (Fig. 4), ion number density contours are indicated as solid lines and electron number density contours as dash-dot-dot lines. These plots support the observation that the radial extent of the discharge is increased with the application of the applied magnetic field. Note also the close correspondence of the ion and electron density contours in the quasi-neutral positive column.

A final interesting feature to note is the appearance of a swirl component of the current density with the application of a strong magnetic field. This phenomenon is illustrated in Fig. 6, which shows the current density components j_y-j_z in the y-z-plane. (Note that every other vector is omitted for clarity.) The swirl component of the current density is zero on the centerline, peaks about 7 mm away, then falls to zero toward the boundaries. The maximum value of the circumferential component of the current density is about 0.27 A/m^2, compared to a maximum axial current density of about 29 A/m^2, which occurs at the anode. These results show the importance of modeling cases with an applied magnetic field in three dimensions.

The calculations considered here show a possible method for stabilizing a discharge. They also illustrate many of the basic features of a glow discharge in the normal glow regime, in which the discharge does not interact with the electrode boundaries. In the application of DC discharges to practical flow control problems, however, the discharge is expected to be in the abnormal region, and the effects of electrode edges and corners must be considered. In the next section, we address this issue, examining a case in which a discharge between finite, rectangular electrodes is present in a laminar, high Mach number, flat plate boundary layer.

IV. Flat Plate

A computational study was made of a configuration similar to that examined experimentally by Kimmel *et al.*[6] The dimensions of the test article considered here are close to, but not exactly the same as, those considered in that study. The working fluid was taken to be nitrogen, rather than air as in the experiments. The test article was a 66 mm × 38.1 mm, sharp-edged flat plate. The freestream conditions were $p_\infty = 64$ Pa, $T_\infty = 43$ K, and $u_\infty = 688$ m/s; adiabatic wall conditions were assumed.

A computational grid of 101 × 81 × 81 points, distributed over a rectangular domain of dimensions 66 mm × 25 mm × 38.1 mm, was considered. The cathode and anode were taken to be located on the plate surface ($y = 0$ mm), with a finite extent in the spanwise direction (9.5 mm $\le z \le$ 28.6 mm). The cathode was located at a station upstream (13.2 mm $\le x \le$ 26.4 mm), and the anode farther downstream (39.6 mm $\le x \le$ 52.8 mm). Grid clustering was employed near the electrode boundaries and near the plate surface. The cathode was held at $\phi = -1$ kV (no external load), and the secondary emission coefficient was taken to be $\gamma = 0.1$.

Figure 7 shows three-dimensional perspective views of the computed solution with the discharge on. Contours of electric potential with selected current lines are shown in Fig. 7a, and corresponding isobars are shown in Fig. 7b. Bulk gas flow is in the positive x-direction, and current flows from the downstream anode to the upstream cathode. The flow of current from anode to cathode is about 0.4 A, and is seen to introduce a significant pressure perturbation that will be examined in detail below.

Figure 8 shows the potential distribution in the symmetry plane ($z = 19$ mm, Fig. 8a) and at the plate surface ($y = 0$ mm, Fig. 8b) for the case with the discharge on. The figures are oriented so that the predominant flow direction is from left to right in each view. In Fig. 8a, the flat plate is situated at the bottom of the plots ($y = 0$ mm), and the locations of the cathode and anode are indicated by filled rectangles just outside the domain of the plot. Figure 8b shows a top view of the plate, and the locations of the electrodes are indicated by open rectangles. As might be expected, most of the potential variation occurs near the surface of the cathode and around its edges.

Figures 9-10 illustrate the effect of the discharge on the temperature field. The orientation of the figures is analogous to that in Fig. 8, and the location of the electrodes is marked in the same way. Figures 9a-

b show the wall temperature distribution for the cases with the discharge off and on, respectively. The temperature is uniform in the spanwise direction in the baseline case, and shows a slow variation in the streamwise direction. With the discharge on, the temperature field changes dramatically, with temperature peaks near the downstream edge of the cathode and near the upstream corners of the anode.

The corresponding data for the symmetry plane are shown in Figs. 10a-b. The shock induced by the hypersonic viscous interaction effect is evident as a diagonal structure from lower left to upper right in these plots, and the downstream growth of the boundary layer can be seen near the wall. Again, the dissipative heating present when the discharge is on leads to high temperatures near the electrodes, and a compression wave system is apparent emanating from the cathode.

An analogous set of plots for the pressure distribution is given in Figs. 11-12. Features corresponding to those present in the temperature distribution are apparent in these plots. Of particular note are the maxima corresponding to compression waves introduced at the cathode and the upstream corners of the anode.

Figures 13-15 show selected profiles through the solution, comparing the baseline case to the case with the discharge on. Figure 13a shows the wall temperature profile, and Fig. 13b the wall pressure profile. For the baseline case with the discharge off (dash-dot-dot line), the pressure distribution shows the expected decrease with streamwise position, and the the adiabatic wall temperature shows a slow increase. With the discharge on (solid line), a strong perturbation of the wall temperature and pressure occurs, starting at the cathode and peaking near its downstream edge. A similar effect appears in the profile of the skin friction coefficient (Fig. 14), with a drop in skin friction over the cathode, and an overshooting recovery downstream.

Figure 15 shows boundary profiles for a station at the middle of the plate ($x = 33$ mm, $z = 19$ mm). The thickness of the boundary layer is seen to increase significantly with the discharge on, with an accompanying increase in the temperature at the insulted wall.

force coefficient	control off	control on	change in magnitude
F_x	8.2×10^{-3}	8.4×10^{-3}	+2%
F_y	-7.3×10^{-2}	-7.7×10^{-2}	+6%

Table 1. Effect of glow discharge on flat plate boundary layer.

Given the changes in pressure and skin friction, it is interesting to assess the overall effect of the discharge on the forces on the plate. The results are given in nondimensional form in Table 1. The force coefficients only consider the forces acting on the wetted (upper) side of the plate, and are defined as $F_i = 2/(A\rho_\infty U_\infty^2) \int \Sigma_{ji} \cdot n_j \, dS$, where A is the area of the plate, $\rho_\infty U_\infty^2/2$ is the freestream dynamic pressure, $\mathbf{n}$ is the unit normal vector, and $\mathbf{\Sigma}$ is the total stress tensor defined in Eq. (4). Despite the initial decrease in skin friction over the cathode, the overshooting recovery leads to a small net increase in drag on the plate. The overall downward force on the plate due to wall pressure increases by about 6% with the discharge on due to the increased flow compression with boundary layer thickening.

The results obtained here are qualitatively consistent with experimental observation of discharges[6,26] and simple heating[26,27] and with computations based on simplified physical models based on gasdynamic heating[28–30] or quasi-neutral electromagnetics.[17,30] Contrasting the present work to the previous computational studies, we see that three-dimensionality may be a more important factor than non-neutrality. The major difference between the present results and those of the previous studies is the observation of strong heating at the corners of the anode.

Examining the source terms that appear in the fluid conservation laws, we find that the changes that the discharge introduces in the flow structure are primarily due to dissipative heating effects, rather than the electric force on the bulk gas. The maximal values of the nondimensional source terms occur near the downstream edge of the cathode, where the electric field is high. The nondimensional electromagnetic power term $P = \eta \mathbf{E} \cdot \mathbf{j} L/(\rho_\infty u_\infty^3)$ has a maximum value of $P \approx 6$. In comparison, the maximum nondimensional rate of mechanical work done by the electric body force $P_m = \rho_c \mathbf{E} \cdot \mathbf{u} L/(\rho_\infty u_\infty^3)$ is three orders of magnitude

smaller: $P_m \approx -0.006$. The maximum nondimensional value of the wall-normal component of the body force $f_y = \rho_c E_y L/(\rho_\infty u_\infty^2)$ is quite small: $f_y \approx -0.04$, and the other force components are completely negligible. Indeed, turning off the force term in the calculations had no discernible effect on the solution.

One would expect the body force and energy deposition source terms to be more significant in low speed flow, since the freestream momentum flux and kinetic energy are lower in comparison. This issue is examined for flow over a low-speed airfoil in the next section.

V. Airfoil

A set of computations was carried out for a NACA-0012 airfoil configuration in order to examine the possibility of controlling low-speed flows using glow discharges. The computational grid consisted of $203 \times 101 \times 5$ points. An 'O-grid' topology was chosen, with a region of five point overlap on the upstream side of the airfoil. The grid was highly clustered to resolve the viscous boundary layer near the airfoil surface. Uniformity was imposed along the z-direction.

As an initial code verification exercise, calculations were carried out for an air flow with a Mach number of $M = 0.2$, a Reynolds number of $\mathrm{Re} = 2500$, and an angle of attack of $\alpha = 1^\circ$. The corresponding dimensional conditions were approximately $p_\infty = 179$ Pa, $T_\infty = 289$ K, $U_\infty = 68$ m/s, and $L_{\mathrm{ref}} = 0.30$ m. The pressure coefficient on the airfoil surface is shown in Fig. 16. The higher pressures correspond to the lower surface of the airfoil. The results of the present calculations using the PS3D code are indicated by a solid line, whereas the symbols represent results obtained for the same grid and flow conditions using a different code. (This code, FDL3DI, is a widely used and well tested viscous flow solver.[31]) The agreement between the codes is seen to be extremely close, lending confidence that the PS3D code is correctly implemented.

A second set of calculations was carried out for a nitrogen flow on the same computational grid. For this case, dimensional freestream conditions were taken to be the same as those in the air flow, so there was a slight difference in the nondimensional conditions from the verification case. The Mach number changed to 0.197 and the Reynolds number to 2494. The angle of attack was $\alpha = 1^\circ$, as before.

Computations were carried out for a baseline flow case, and for a case with a DC discharge over the upper surface of the airfoil. For the discharge case, the cathode was fixed at -500 V, and was located on the upper surface of the airfoil in the range -0.075 mm $\leq x \leq -0.065$ m. The anode was fixed at 0 V, and was located on the upper surface of the airfoil in the range 0.220 m $\leq x \leq 0.226$ m.

The basic glow discharge properties are illustrated in Fig. 17. The number density distribution is shown in Fig. 17a and contours of the electric potential are shown in Fig. 17b, along with selected current lines. Strong ionization is seen to be confined to the vicinity of the electrodes, and the bulk of the electric current flows from anode to cathode along the upper surface of the airfoil. A portion of the current, however, follows a longer path around the underside of the airfoil. The net current is about 0.9 A/m. (Since the computation is two-dimensional, this figure is per meter in the z-direction.)

The effect of the discharge on the temperature distribution is shown in Fig. 18. In the baseline case (Fig. 18a), the presence of the airfoil introduces only a small perturbation in the freestream flow - on the order of 2 K. With the discharge on (Fig. 18b), a significant increase in temperature (up to ~ 60 K) is observed, primarily in the vicinity of the electrodes and their downstream thermal wakes.

This heating has an effect on the pressure field, as seen in Fig. 19. The pressure field is seen to remain qualitatively the same, with quantitative differences in the flow structure. This change is more evident in the distributions of the surface pressure coefficient and the skin friction coefficient, which are shown in Fig. 20. The effect of the discharge is to moderate the pressure distribution: it decreases the pressure on the underside of the airfoil and increases the pressure on the upper side (Fig. 20a). Plasma control also slightly increases the skin friction coefficient over the whole airfoil (Fig. 20b).

The net result is an overall decrease in airfoil performance when the discharge is on. Data for the lift and drag coefficients are shown in Table 2, where the lift coefficient is defined as $C_L = 2L/(A\rho_\infty U_\infty^2)$ and the drag coefficient as $C_D = 2D/(A\rho_\infty U_\infty^2)$. We observe a small increase in the drag on the airfoil, and a substantial decrease in lift, with a corresponding decrease of about 18% in the lift to drag ratio.

force coefficient	control off	control on	change
C_D	7.6×10^{-2}	7.9×10^{-2}	+3%
C_L	4.6×10^{-2}	3.9×10^{-2}	-15%
L/D	0.60	0.50	-18%

Table 2. Effect of glow discharge on NACA-0012 airfoil flow.

Although this effect might have an application in flight control, flow control based on heat release may be not be as useful in general for very low speed flows as in a higher speed regime. Indeed, decreased drag has been observed in experiments on airfoil shapes[32] and wing-fuselage bodies[33] in transonic flow. In the low speed regime, dielectric barrier discharges, which generate significant electric body forces on the gas flow, appear to be very promising for flow control.[3,4,34]

As expected, higher values of the nondimensional source terms occur for this subsonic flow, but large values of the source terms are confined to a region in the vicinity of the edges of the cathode. The maximum magnitude of the nondimensional force is on the order of $f \approx 40$, the corresponding nondimensional mechanical power is about $P_m \approx 0.05$, and the nondimensional total power term is on the order of $P \approx 5000$. Further numerical study is needed to determined whether this region is adequately resolved in the present computation.

VI. Summary and Discussion

Over the past several years, a program has been underway to develop a capability to numerically simulate experiments with plasma actuators and evaluate their potential for flow control applications. Towards this end, a three-dimensional computer code has been written to solve, in an implicit, loosely-coupled fashion, the fluid conservation laws, the charged particle continuity equations under the drift-diffusion model, and the Poisson equation for the electric potential. Earlier efforts considered simple two-dimensional, direct-current glow discharges, then considered more complicated geometries with uncoupled fluid mechanics. In the present work, we have moved on to fully three-dimensional calculations with full coupling of the discharge to the flow through the body force and energy deposition source terms.

The first case examined in the present work was a fully three-dimensional computation of a simple direct-current glow discharge between parallel plates. For the baseline case, features were observed that are consistent with standard results in the normal glow regime. These included a strong potential drop near the cathode surface, a peak in the ion number density near the cathode that is an order of magnitude larger than the plasma density in the positive column, and the discharge current occupying only a portion of the electrode surfaces. A preliminary investigation of the effect of an applied magnetic field showed that the field tends to suppress the radial component of the current density and introduce a small swirl component.

With this validation case completed, changes in the flow with the presence of a discharge were demonstrated. In computations of a three-dimensional electrode configuration mounted on a flat plate in a Mach 5 crossflow, the effect of the discharge was to thicken the boundary layer. The resulting compression waves led to increased pressure forces at the plate surface. These changes in flow structure occurred through dissipative heating; the body force term in the fluid momentum equation was negligible. Nevertheless, this form of flow control may be useful for high-speed applications, where conventional mechanical control surfaces are often unsuitable.

Analogous, but less dramatic effects, were observed for electrodes mounted on a NACA-0012 airfoil in low-speed flow. Here the net result was a decrease in airfoil performance: a moderate increase in drag and a substantial decrease in lift. Again, the changes in the flow came about primarily through dissipative heating. Although this effect might have an application in flight control, flow control based on heat release may be

not be as useful in general for very low speed flows as in a higher speed regime.

Acknowledgments

This project is sponsored in part by the Air Force Office of Scientific Research (monitored by J. Schmisseur and F. Fahroo), and by a grant of High Performance Computing time from the Department of Defense Major Shared Resource Centers at the Army High Performance Computing Research Center (AHPCRC) and the Aeronautical Systems Center (ASC). The author would like to acknowledge helpful discussions of the present work with D. Gaitonde, N. Sternberg, and M. White.

References

[1]Bychkov, V., Kuz'min, G., Minaev, I., Rukhadze, A., and Timofeev, I., "Sliding Discharge Application in Aerodynamics," AIAA Paper 2003-0530, January 2003.

[2]Enloe, C. L., McLaughlin, T. E., VanDyken, R. D., Kachner, K. D., Jumper, E. J., and Corke, T. C., "Mechanisms and Responses of a Single Dielectric Barrier Plasma," AIAA Paper 2003-1021, January 2003.

[3]Post, M. L. and Corke, T. C., "Separation Control on High Angle of Attack Airfoil Using Plasma Actuators," AIAA Paper 2003-1024, January 2003.

[4]Roth, J. R., Sin, H., Madhan, R. C. M., and Wilkinson, S. P., "Flow Re-attachment and Acceleration by Paraelectric and Peristaltic Electrohydrodynamic (EHD) Effects," AIAA Paper 2003-0531, January 2003.

[5]Wilkinson, S. P., "Investigation of an Oscillating Surface Plasma for Turbulent Drag Reduction," AIAA Paper 2003-1023, January 2003.

[6]Kimmel, R. L., Hayes, J. R., Menart, J. A., and Shang, J., "Effect of Surface Plasma Discharges on Boundary Layers at Mach 5," AIAA Paper 2004-0509, January 2004.

[7]Meyer, R., Chintala, N., Bystricky, B., Hicks, A., Cundy, M., Lempert, W. R., and Adamovich, I. V., "Lorentz Force Effect on a Supersonic Ionized Boundary Layer," AIAA Paper 2004-0510, January 2004.

[8]Wie, D. M. V., Risha, D. J., and Suchomel, C. F., "Research Issues Resulting from an Assessment of Technologies for Future Hypersonic Aerospace Systems," AIAA Paper 2004-1357, January 2004.

[9]Poggie, J. and Gaitonde, D. V., "Electrode Boundary Conditions in Magnetogasdynamic Flow Control," AIAA Paper 2002-0199, January 2002.

[10]Poggie, J., Gaitonde, D. V., and Sternberg, N., "Numerical Simulation of Plasma Sheaths in Aerodynamic Applications," AIAA Paper 2002-2166, May 2002.

[11]Poggie, J., "Numerical Simulation of Electromagnetic Flow Control for Hypersonic Systems," AIAA Paper 2002-5182, October 2002.

[12]Poggie, J. and Sternberg, N., "Numerical Simulation of Electrode Sheaths in a Magnetized Plasma," AIAA Paper 2003-0359, January 2003.

[13]Poggie, J. and Sternberg, N., "Numerical Simulation of Glow Discharges for High-Speed Flow Control," AIAA Paper 2004-0177, January 2004.

[14]Sternberg, N. and Poggie, J., "Plasma-Sheath Transition in the Magnetized Plasma-Wall Problem for Collisionless Ions," *IEEE Transactions on Plasma Science*, Vol. 32, No. 6, 2004, pp. 2217–2226.

[15]Poggie, J., "Numerical Exploration of Flow Control with Glow Discharges," AIAA Paper 2004-2658, June 2004.

[16]Poggie, J. and Sternberg, N., "Transition from the Constant Ion Mobility Regime to the Ion-Atom Charge-Exchange Regime for Bounded Collisional Plasmas," *Physics of Plasmas*, Vol. 12, No. 2, Feb. 2005, to appear.

[17]Shang, J. S. and Surzhikov, S. T., "Magneto-Fluid-Dynamics Interaction for Hypersonic Flow Control," AIAA Paper 2004-0508, January 2004.

[18]White, F. M., *Viscous Fluid Flow*, McGraw-Hill, New York, 2nd ed., 1991.

[19]Surzhikov, S. T. and Shang, J. S., "Two-Component Plasma Model for Two-Dimensional Glow Discharge in Magnetic Field," *Journal of Computational Physics*, Vol. 199, 2004, pp. 437–464.

[20]Beam, R. and Warming, R., "An Implicit Factored Scheme for the Compressible Navier-Stokes Equations," *AIAA Journal*, Vol. 16, No. 4, 1978, pp. 393–402.

[21]Pulliam, T. H., "Implicit Finite-Difference Simulations of Three-Dimensional Compressible Flow," *AIAA Journal*, Vol. 18, No. 2, 1980, pp. 159–167.

[22]Jameson, A., Schmidt, W., and Turkel, E., "Numerical Solutions of the Euler Equations by a Finite Volume Method Using Runge-Kutta Time Stepping Schemes," AIAA Paper 81-1259, 1981.

[23]Holst, T. L., "On Approximate Factorization Schemes for Solving the Full Potential Equation," NASA TM 110435, 1997.

[24]Holst, T. L., "Transonic Flow Computations Using Nonlinear Potential Methods," *Progress in Aerospace Sciences*, Vol. 36, 2000, pp. 1–61.

[25]Chandra, R., Dagum, L., Kohr, D., Maydan, D., McDonald, J., and Menon, R., *Parallel Programming in OpenMP*, Academic Press, 2001.

[26]Menart, J., Henderson, S., Atzbach, C., Shang, J., Kimmel, R., and Hayes, J., "Study of Surface and Volumetric Heating Effects in a Mach 5 Flow," AIAA Paper 2003-2262, June 2003.

[27]Debiève, J.-F., Dupont, P., Smith, D. R., and Smits, A. J., "Supersonic Turbulent Boundary Layer Subject to Step Changes in Wall Temperature," *AIAA Journal*, Vol. 35, No. 1, 1997, pp. 51–57.

[28]Levin, V. A. and Larin, O. B., "Skin-Friction Reduction by Energy Addition into a Turbulent Boundary Layer," AIAA Paper 2003-0036, January 2003.

[29]Leonov, S., Yarantsev, D., Kuryachii, A., and Yuriev, A., "Study of Friction and Separation Control by Surface Plasma," AIAA Paper 2004-0512, January 2004.

[30]Shang, J. S., Gaitonde, D. V., and Updike, G. A., "Modeling Magneto-Aerodynamic Actuator for Hypersonic Flow Control," AIAA Paper 2004-2657, June 2004.

[31]Rizzetta, D. P. and Visbal, M. R., "Application of Large-Eddy Simulation to Supersonic Compression Ramps," *AIAA Journal*, Vol. 40, No. 8, 2002, pp. 1574–1581.

[32]Leonov, S., Bityurin, V., Savischenko, N., Yuriev, A., and Gromov, V., "Influence of Surface Electrical Discharge on Friction of Plate in Subsonic and Transonic Airflow," AIAA Paper 2001-0640, January 2001.

[33]Skvortsov, V., Kuznetsov, Y., Klimov, A., Leonov, S., Markin, V., and Uspenskii, A., "Investigation of the Plasma Aerodynamic Effects on the Models of Various Geometry," AIAA Paper 99-4854, June 1999.

[34]Roy, S. and Gaitonde, D., "Radio Frequency Induced Ionized Collisional Flow Model for Application at Atmospheric Pressures," *Journal of Applied Physics*, Vol. 96, No. 5, 2004, pp. 2476–2481.

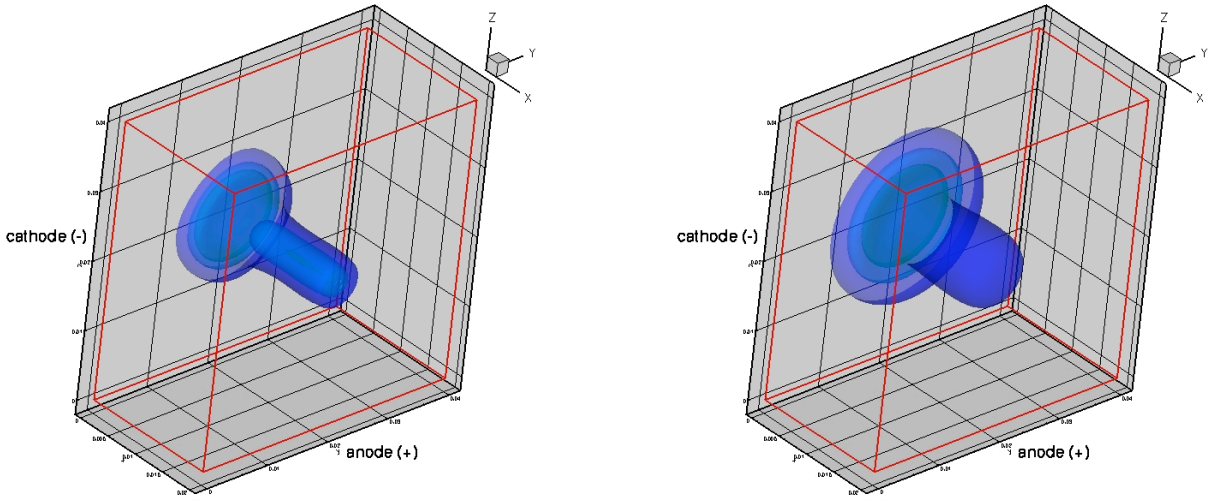

(a) No magnetic field, $B = 0$.

(b) Applied magnetic field, $B_x = 1$ T.

Figure 1. Glow discharge - ion number density isosurfaces. Isosurfaces: $1 \times 10^{15}\mathrm{m}^{-3}$**,** $5 \times 10^{15}\mathrm{m}^{-3}$**,** $1 \times 10^{16}\mathrm{m}^{-3}$**.**

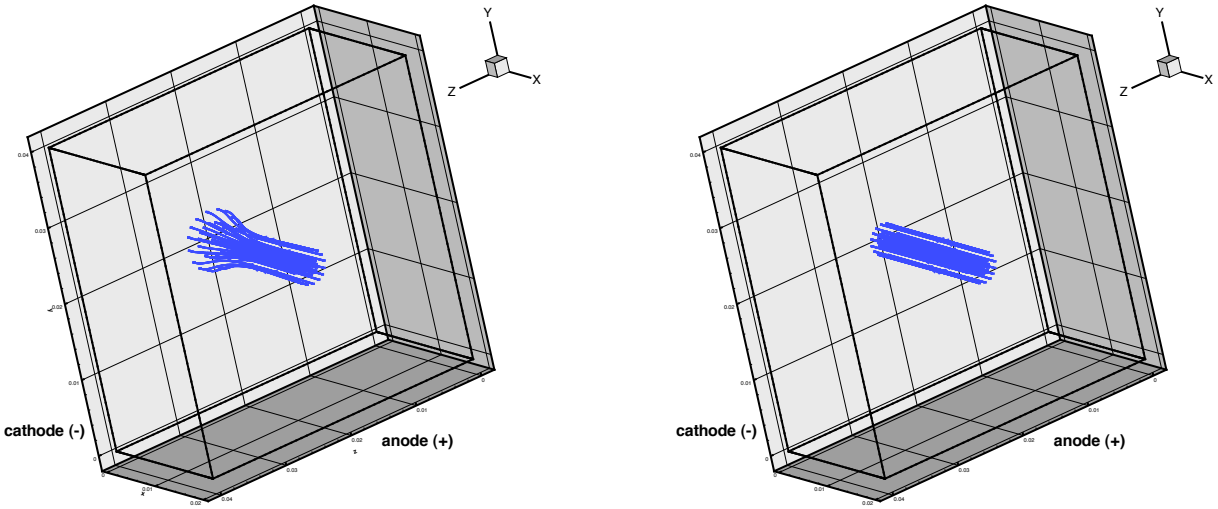

(a) No magnetic field, $B = 0$.

(b) Applied magnetic field, $B_x = 1$ T.

Figure 2. Glow discharge - current lines.

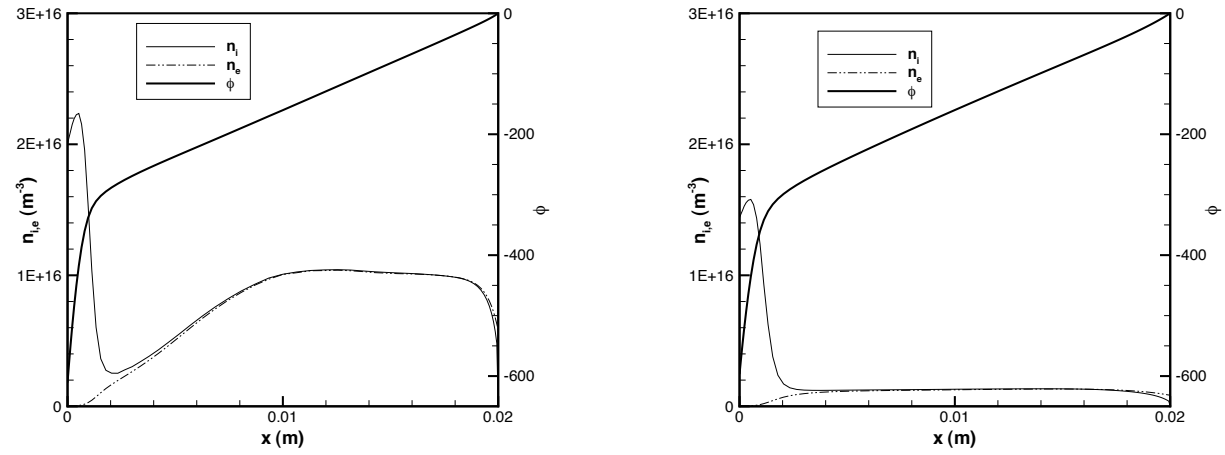

(a) No magnetic field, $B = 0$.

(b) Applied magnetic field, $B_x = 1$ T.

Figure 3. Glow discharge - centerline properties.

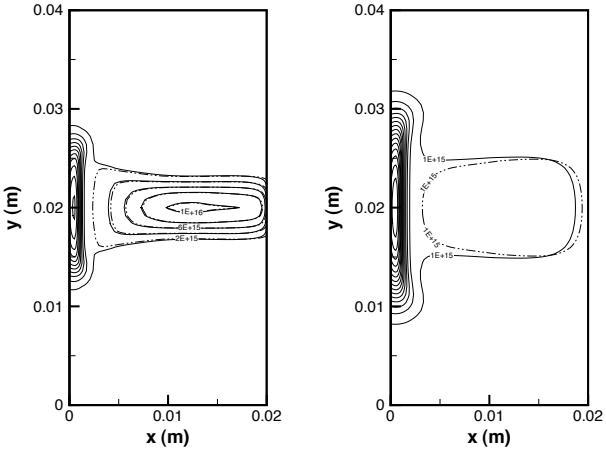

(a) No magnetic field, $B = 0$.

(b) Applied magnetic field, $B_x = 1$ T.

Figure 4. Glow discharge - number densities in x-y-plane.

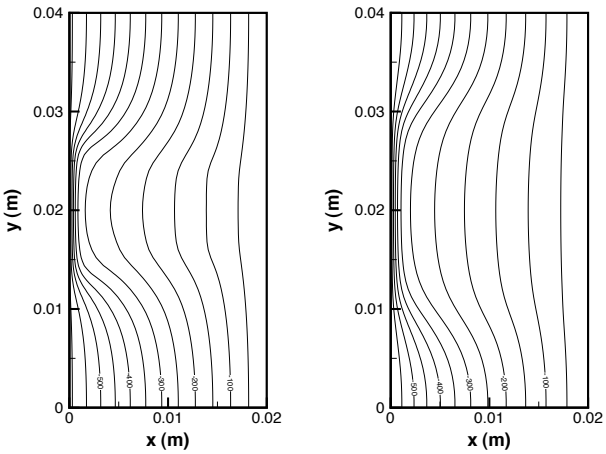

(a) No magnetic field, $B = 0$.

(b) Applied magnetic field, $B_x = 1$ T.

Figure 5. Glow discharge - electric potential in x-y-plane.

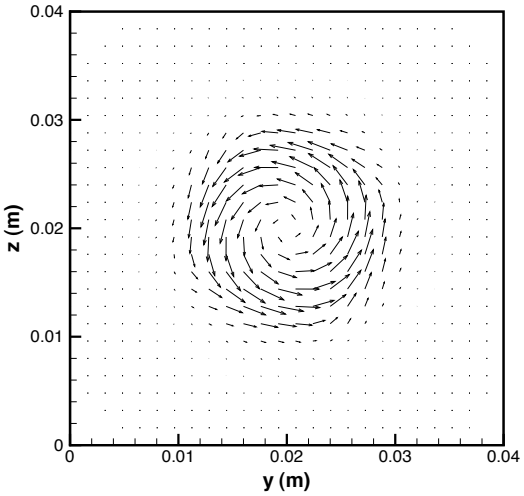

Figure 6. Glow discharge, magnetic field of $B_x = 1$ T - vector components j_y-j_z in y-z-plane. Every other vector omitted for clarity.

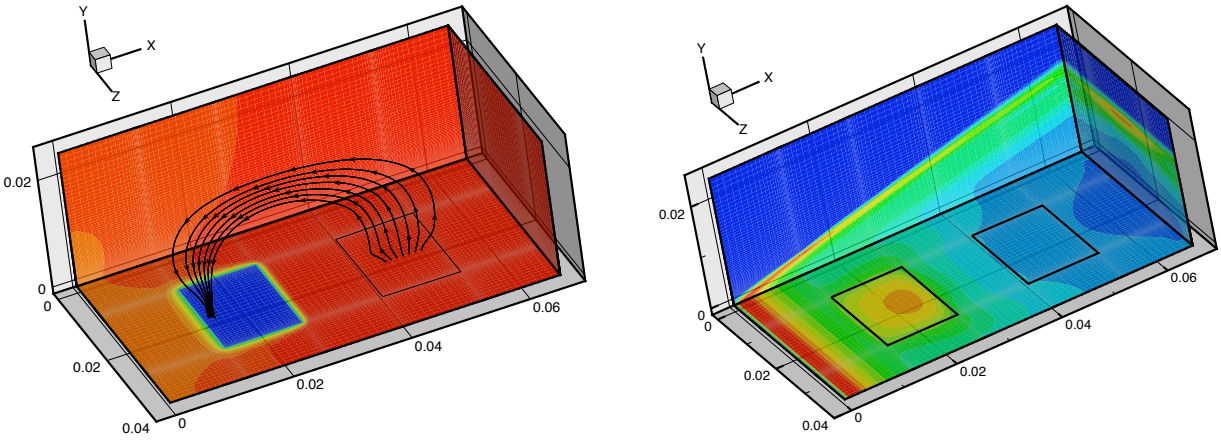

(a) Potential distribution with selected current lines.

(b) Pressure distribution.

Figure 7. Glow discharge in flat plate boundary layer, with finite electrodes.

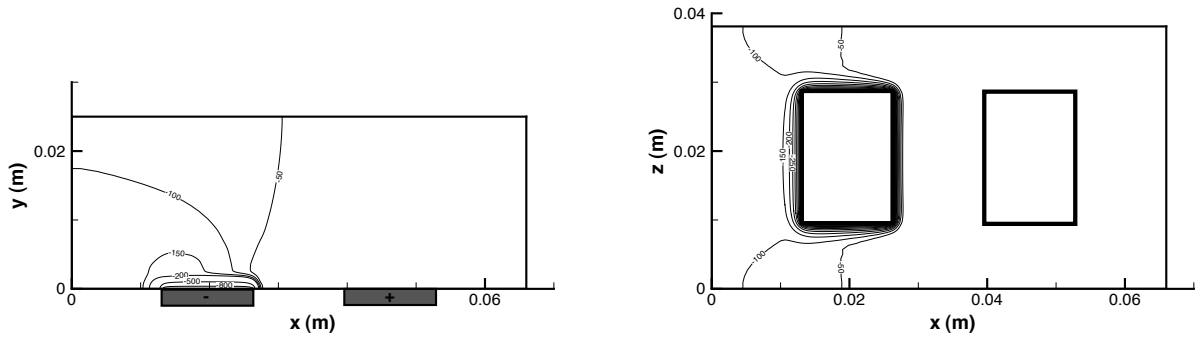

(a) Symmetry plane, $z = 19$ mm.

(b) Plate surface, $y = 0$ mm.

Figure 8. Potential distribution (V) with discharge on.

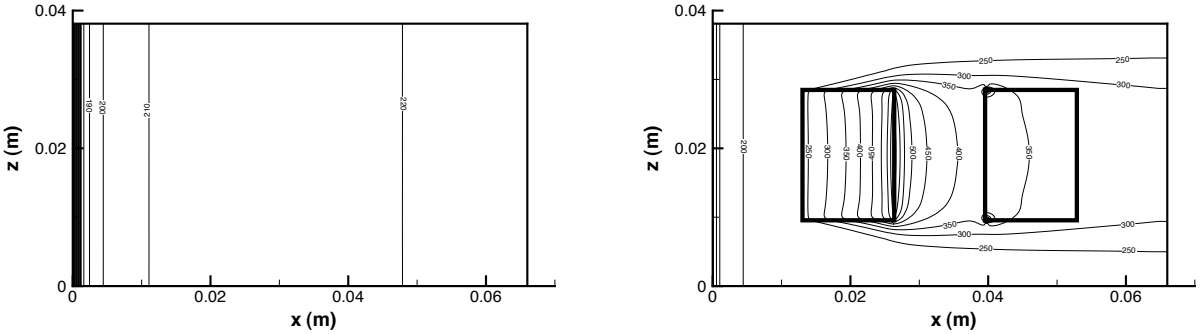

(a) Baseline case. (b) Discharge on.

Figure 9. Effect of discharge on wall temperature distribution (K).

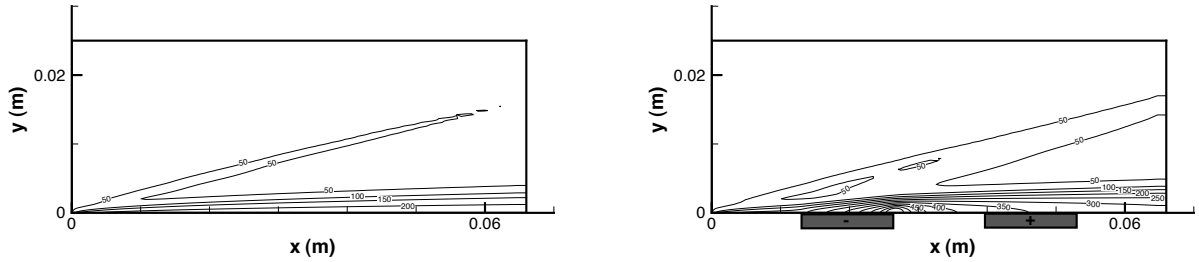

(a) Baseline case. (b) Discharge on.

Figure 10. Effect of discharge on symmetry plane temperature distribution (K).

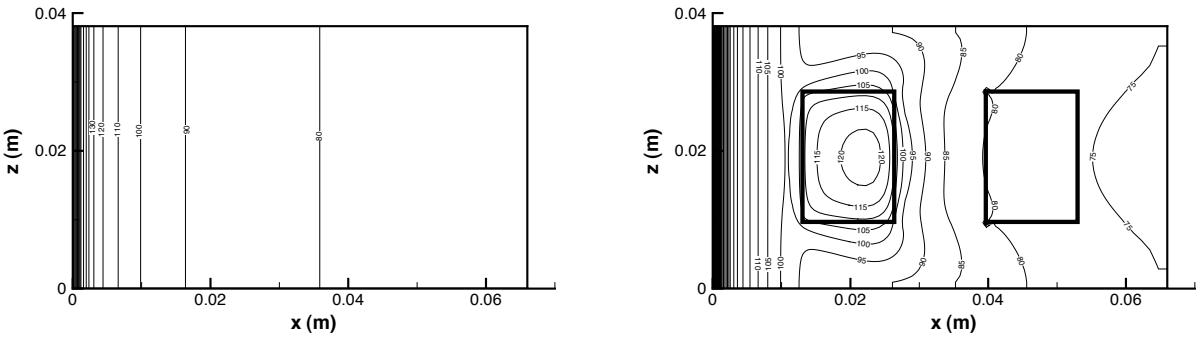

(a) Baseline case. (b) Discharge on.

Figure 11. Effect of discharge on wall pressure distribution (Pa).

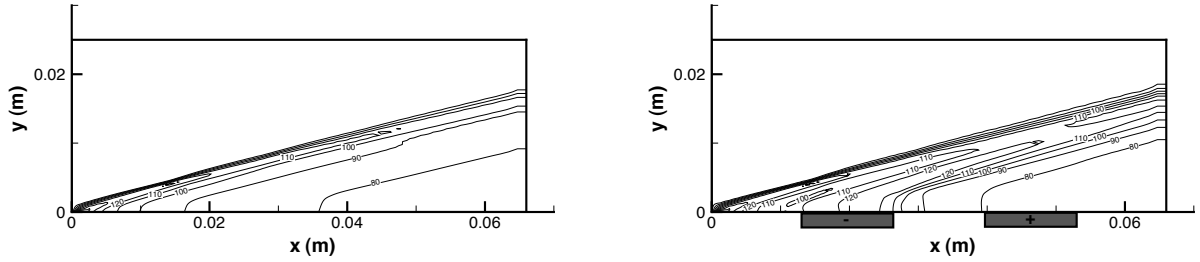

(a) Baseline case.

(b) Discharge on.

Figure 12. Effect of discharge on symmetry plane pressure distribution (Pa).

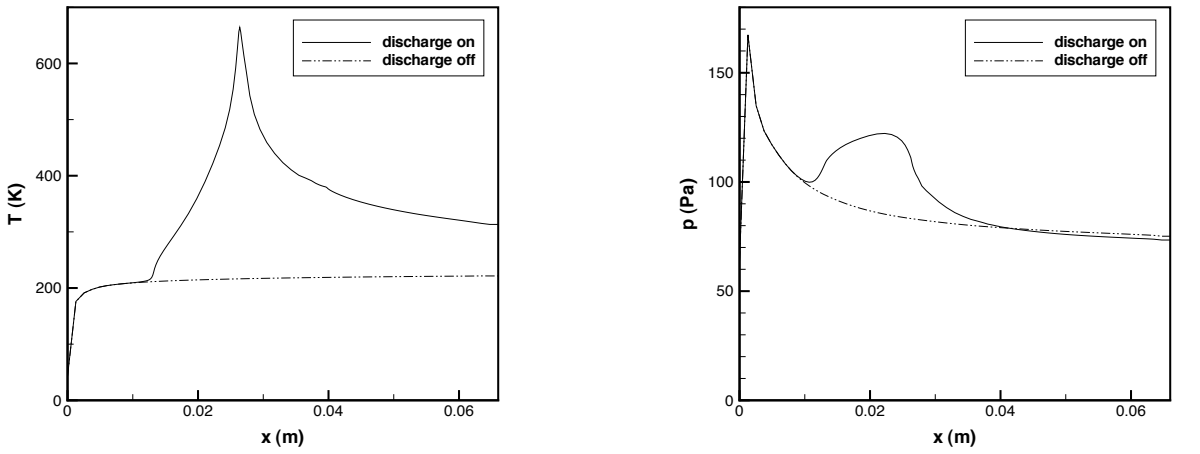

(a) Temperature distributions on line $y = 0$ mm, $z =$ 19 mm.

(b) Pressure distributions on line $y = 0$ mm, $z =$ 19 mm.

Figure 13. Flat plate boundary layer with finite electrodes - selected profiles.

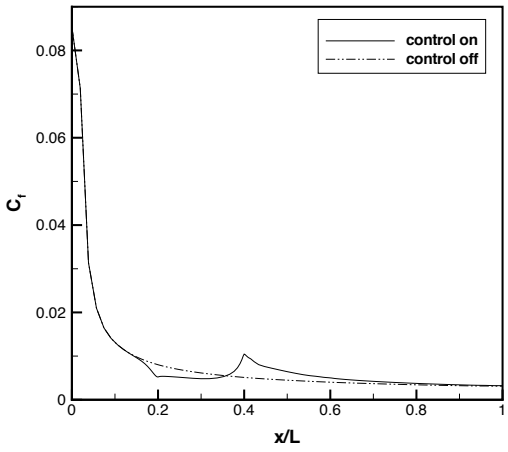

Figure 14. Flat plate boundary layer with finite electrodes - skin friction coefficient on line $y = 0$ mm, $z = 19$ mm.

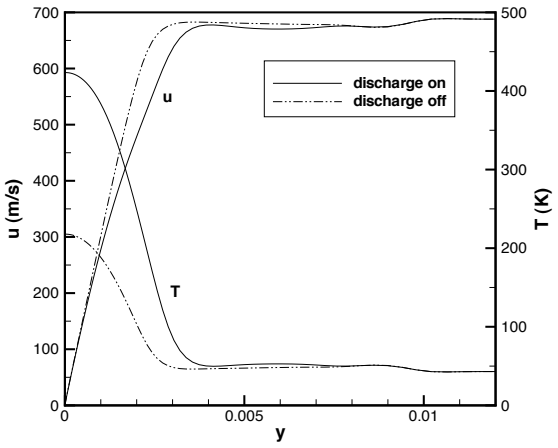

Figure 15. Flat plate boundary layer with finite electrodes - boundary layer profiles for $x = 33$ mm, $z = 19$ mm.

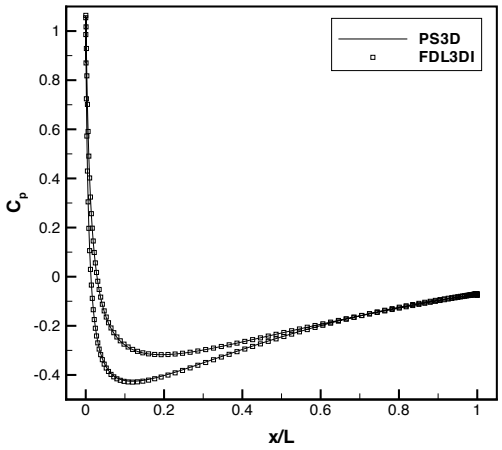

Figure 16. Computed pressure coefficient on airfoil surface: results for PS3D and FDL3DI codes. Air flow, $\mathrm{Ma} = 0.2$, $\mathrm{Re} = 2500$, $\alpha = 1°$.

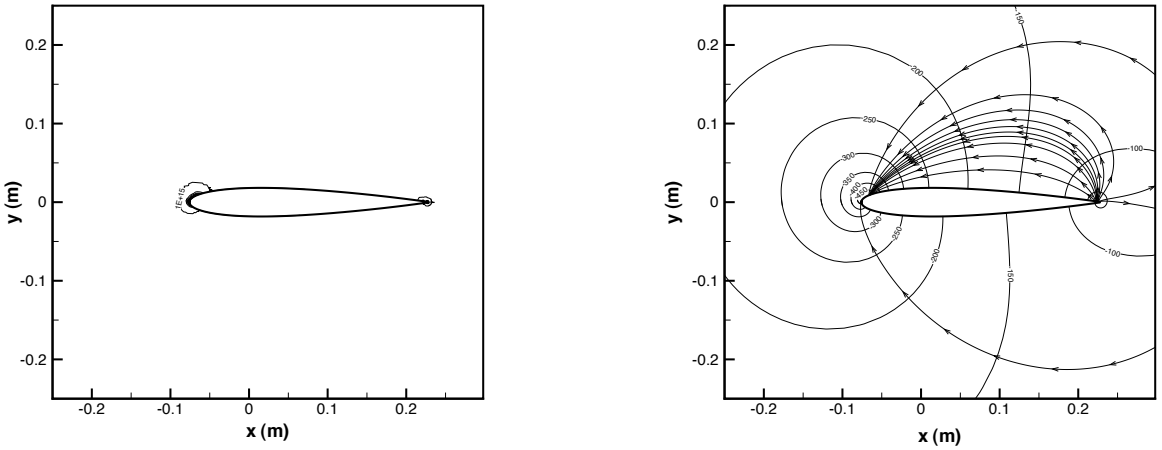

(a) Number densities.

(b) Electric potential and current lines.

Figure 17. Discharge properties for NACA-0012 airfoil.

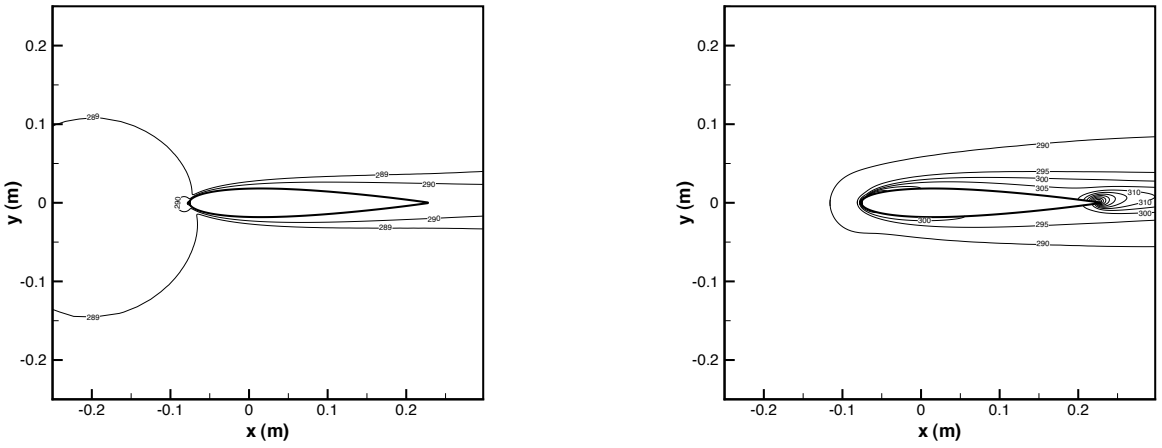

(a) Discharge off.

(b) Discharge on.

Figure 18. Temperature distribution in flow over NACA-0012 airfoil.

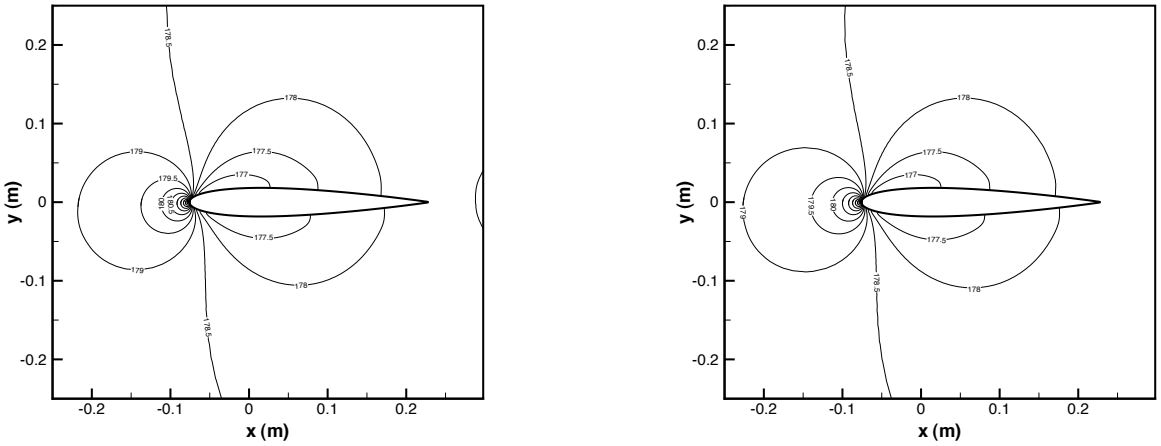

(a) Discharge off.

(b) Discharge on.

Figure 19. Pressure distribution in flow over NACA-0012 airfoil.

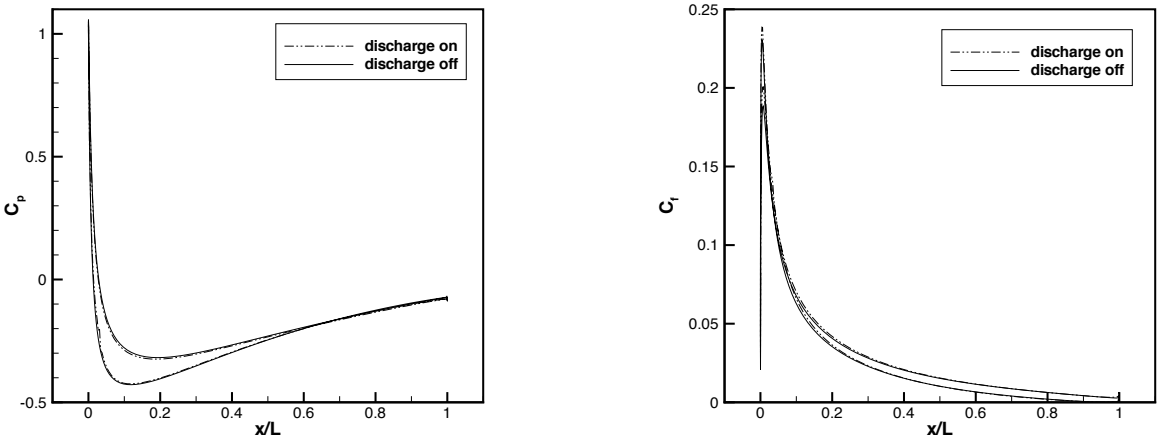

(a) Pressure coefficient.

(b) Skin friction coefficient.

Figure 20. Effect of discharge on surface properties in flow over NACA-0012 airfoil.